

Inference and Interference: The Role of Clipping, Pruning and Loss Landscapes in Differentially Private Stochastic Gradient Descent

Lauren Watson,¹ Eric Gan,² Mohan Dantam,¹ Baharan Mirzasoleiman,² Rik Sarkar¹

¹School of Informatics, University of Edinburgh

²University of California, Los Angeles

lauren.watson@ed.ac.uk, baharan@cs.ucla.edu, rsarkar@inf.ed.ac.uk

Abstract

Differentially private stochastic gradient descent (DP-SGD) is known to have poorer training and test performance on large neural networks, compared to ordinary stochastic gradient descent (SGD). In this paper, we perform a detailed study and comparison of the two processes and unveil several new insights. By comparing the behavior of the two processes separately in early and late epochs, we find that while DP-SGD makes slower progress in early stages, it is the behavior in the later stages that determines the end result. This separate analysis of the clipping and noise addition steps of DP-SGD shows that while noise introduces errors to the process, gradient descent can recover from these errors when it is not clipped, and clipping appears to have a larger impact than noise. These effects are amplified in higher dimensions (large neural networks), where the loss basin occupies a lower dimensional space. We argue theoretically and using extensive experiments that magnitude pruning can be a suitable dimension reduction technique in this regard, and find that heavy pruning can improve the test accuracy of DP-SGD.

1 INTRODUCTION

The wide-ranging potential applications of deep learning models trained on large datasets has recently raised concerns about the privacy properties of these models. The current method to enforce privacy while training such models is differential privacy (Dwork, 2006). The

most popular of these methods is Differentially Private Stochastic Gradient Descent (DP-SGD) (Abadi et al., 2016). By restricting the maximum gradient norm and adding suitable noise at every step of ordinary Stochastic Gradient Descent (SGD), it ensures the rigorous privacy properties of differential privacy and defends against privacy attacks (Shokri et al., 2017; Fredrikson et al., 2015; Nasr et al., 2019; Carlini et al., 2019).

The perturbations produced by noise addition and gradient clipping come at the cost of reduced utility, and the practical performance of DP-SGD – as measured by common loss and accuracy measures – is found to be consistently inferior to that of SGD, even on standard benchmark tasks (Papernot et al., 2021). This gap is governed by several entities including the class of models, the gradients generated by SGD, the perturbation induced by DP-SGD, and the *loss landscape* over the space of models \mathcal{H} where the training process takes place. The relations between these entities are complex, and are the subject of this paper. It has been conjectured that the primary weakness of DP-SGD is in the early rounds, where the noise may inhibit it from identifying a good basin (Ganesh et al., 2023) within the loss landscape. Having missed the opportunity, it is constrained to the quality of the basin it finds. On the other hand, studies on the SGD process have found that it is often possible to arrive at equally good minima from different starting points of SGD (Frankle et al., 2020) and for some common learning tasks, these different loss basin floors are connected (Garipov et al., 2018). The performance of DP-SGD is known to deteriorate with the dimension of \mathcal{H} , or equivalently, with the number of parameters of the model, since to privatize a greater number of parameters requires greater noise. Thus, several methods have been proposed to reduce the number of parameters by pruning, gradient sparsification and others (Luo et al., 2021; Li et al., 2022; Zhou et al., 2021).

1.1 Contributions

We provide several insights into the behavior of DP-SGD by comparing it with the fine grained behavior of ordinary SGD. The results include observations about the nature of the loss basins, why DP-SGD fails to find a floor (minimum) of the basin as effectively as SGD does, how clipping and noise addition contribute to the process, and how pruning improves the performance. Below, we summarize these findings.

If the early rounds of training are decisive, as suggested in (Ganesh et al., 2023) then the process – SGD or DP-SGD – used in the first few (say k epochs) will determine the quality of the model, irrespective of the process operating in later epochs. To test this idea, we divided the T step training process into Phase 1 (first k epochs) and Phase 2 (remaining $T - k$ epochs). Then four models were trained corresponding to using SGD or DP-SGD in each of the phases. The results consistently show that the process used in Phase 2 has a larger impact. In Figure 2, the loss and accuracy levels at the end of Phase 1 are clearly different for SGD and DP-SGD. But in Phase 2, the results change, so that the SGD processes in Phase 2 converge to similar low losses, while the processes running DP-SGD in Phase 2 converge to higher loss. Thus, contrary to the conjecture in Ganesh et al. (2023), it is the Phase 2 process that is decisive, suggesting that the perturbations prevent DP-SGD from finding a good solution irrespective of initial steps. Similar results on other models are found in Section 4.

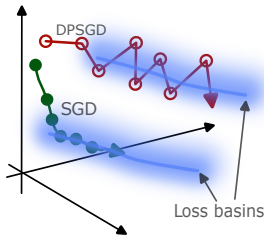


Figure 1: Loss Basins with 1-D Basin floors (shown as blue lines). Loss basin dimension is low compared to ambient dimension. SGD finds and stays at the floor. DP-SGD finds it hard to stay at the floor as the large magnitude of random noise easily throws it far from the floor, and loss increases rapidly in random directions.

Next, we turn to studying the loss landscape and loss basins that guide the training process. In experiments (also seen in (Frankle et al., 2020; Garipov et al., 2018)), SGD usually finds a model at the floor (or plateau) of a loss basin. At the floor, there are a few directions where the loss stays flat. We find that in most other directions, the loss rises rapidly. The conclusion from this result is that while the ambient dimension (the number of

parameters or weights) of a neural network is large, a loss basin lies only in a relatively lower dimensional subspace. The idea is shown schematically in Figure 1, where one dimensional loss basins are embedded in 3D space. In almost any direction from a basin floor, the loss rises rapidly. When the number of orthogonal dimensions are larger, the effect is more pronounced, and has major consequences for DP-SGD: since the noise induced by DP-SGD is a random vector drawn from a high dimensional Gaussian, and therefore of large magnitude. The result is that DP-SGD cannot find the basin floor or remain close to it. (Figure 1).

Further, even with quite short lengths of Phase 1, SGD can find its basin, after which SGD processes end on the same basin floor. However, when DP-SGD is used in Phase 2, processes usually do not end in the same basin. In fact, in many cases, DP-SGD jumps from one basin to another. Even when models do converge to the same basin, DP-SGD does not find a floor that SGD does consistently.

We then examine the effects of clipping and noise addition separately. In experiments, while SGD can tolerate noise addition of the same scale as that required to guarantee $\epsilon = 1$ differential privacy, clipping to the same level as an $\epsilon = 1$ DP-SGD model significantly reduces SGD test accuracy. We use analysis at both small scales (a few training steps) and larger scales (a full training run) to provide evidence that the clipping operation prevents the DP-SGD model from recovering from noise addition that would otherwise have little impact on the training ability for the model.

Given this understanding of the low dimensional loss basins, and the impact of clipping and noise addition on finding these solutions, we show that suitable pruning can mitigate these effects. As with previous work ((Luo et al., 2021)) we find that appropriate pruning improves the accuracy of DP-SGD and that pruned DP-SGD models better replicate the low dimensional behavior of SGD models. Even when the pruning is carried out using only 5% of the data or with a different dataset, DP-SGD on the pruned network generalizes better than DP-SGD on the full network. Separate experiments on clipping and noise addition show that pruning significantly reduces the impact of the clipping operation.

Theoretically, while it is clear from previous work that the effect of noise increases with the number of parameters (Bassily et al., 2014) and therefore pruning will reduce the impact of noise, the effect of clipping and the corresponding potential benefits of pruning are less immediate. We show that pruning can in fact reduce the harmful effects of clipping, by defining a term R based on the variance along each dimension and the

true gradient norm, which decreases with improvement in clipped gradient. The reduction of this term with pruning is verified empirically.

2 TECHNICAL BACKGROUND

2.1 Differential privacy and Stochastic Gradient Descent

Differential privacy as outlined in Definition 2.2 guarantees that the presence or absence of a single datapoint in the underlying training dataset will have a limited impact on the output model, with lower values of ϵ corresponding to stronger privacy guarantees.

Definition 2.1 (Neighboring Databases). Two databases D, D' are neighboring if $H(D, D') \leq 1$, where $H(\cdot, \cdot)$ represents the hamming distance.

Definition 2.2 (Differential Privacy (Dwork, 2006)). A randomized algorithm M satisfies (ϵ, δ) -differential privacy if for all neighboring databases D and D' and for all possible outputs $O \subseteq \text{Range}(M)$, $\Pr[M(D) \in O] \leq e^\epsilon \cdot \Pr[M(D') \in O] + \delta$

Differentially private algorithms often rely on carefully calibrated noise addition to provably ensure differential privacy (Dwork et al., 2006). Abadi et al. (2016) introduced a differentially private variant of the stochastic gradient descent algorithm (DP-SGD). Given data distribution $\mathcal{Z} = \mathcal{X} \times \mathcal{Y}$, loss function $L : (\theta, \mathbf{z}) \rightarrow \mathbb{R}$ for any $\mathbf{z} \in \mathcal{Z}$, learning rate $\eta \in \mathbb{R}^+$, and model parameters θ_t at training step t , SGD calculates the gradient $\mathbf{g}_t = \nabla_{\theta_t} L(\theta_t, \mathbf{z})$ and updates the model parameters to $\theta_{t+1} = \theta_t - \eta \mathbf{g}_t$. In contrast, DP-SGD performs each update step with a perturbed gradient, $\tilde{\mathbf{g}}_t$. The perturbation of the true gradient follows two distinct steps. Firstly, the gradient norm of \mathbf{g}_t is clipped to have maximum norm C , with $\hat{\mathbf{g}}_t = \frac{\mathbf{g}_t}{\max(1, \|\mathbf{g}_t\|_2)}$. Then Gaussian noise with scale σ is added where σ is determined by the required privacy guarantee ϵ , with $\tilde{\mathbf{g}}_t = \hat{\mathbf{g}}_t + \mathcal{N}(0, C\sigma^2\mathbb{I})$. Finally, the update is performed: $\theta_{t+1} = \theta_t - \eta \tilde{\mathbf{g}}_t$.

2.2 Linear mode connectivity

Loss basins that contain different models (say, θ_0 and θ_1) can be compared using a technique called Linear Mode Connectivity (Frankle et al., 2020). In this technique, the loss values are computed for convex combinations of the two models: $(1 - \alpha) * \theta_0 + \alpha \theta_1$ for $\alpha \in [0, 1]$, that lie along the linear segment joining the two models. In practice losses are computed at discrete points, usually 30 (Frankle et al., 2020). Figure 3 shows the typical such linear mode loss profile for two SGD models. The differences in initialization and inherent randomness in SGD data processing can cause the models to end in

different basins with higher loss in between, as seen. It has been shown by (Garipov et al., 2018) that the loss basins may be connected via non-linear paths. The linear mode connectivity technique is best suited to find models that are in the same linearly connected (convex) parts of a basin – where the loss profile at all interpolated points are below some threshold above the loss at the end points, that is, there is no pronounced peak of loss in between the models. The height of this peak loss relative to the loss at the end points is called the *instability* of the training process. More formally, suppose $\mathcal{E}(\theta)$ is the training or test loss for model θ and $\mathcal{E}_\alpha(\theta_0, \theta_1) = \mathcal{E}((1 - \alpha)\theta_0 + \alpha\theta_1)$ for $\alpha \in [0, 1]$ is the loss for a convex combination of the two models.

Definition 2.3 (Linear Interpolation Instability). Let $\mathcal{E}_{sup}(\theta_0, \theta_1) = \sup_\alpha \mathcal{E}_\alpha(\theta_0, \theta_1)$ be the highest loss attained while interpolating between models θ_0 and θ_1 with $\alpha \in [0, 1]$. Let $\bar{\mathcal{E}}_\alpha(\theta_0, \theta_1) = \text{Mean}(\mathcal{E}(\theta_0), \mathcal{E}(\theta_1))$ represent the mean loss of these models. Then the *linear interpolation instability* is given by $\mathcal{E}_{sup}(\theta_0, \theta_1) - \bar{\mathcal{E}}_\alpha(\theta_0, \theta_1)$.

High values of instability caused by a peak as in Figure 3, imply that the models do not both lie on the floor of the same local basin.

3 THEORETICAL ANALYSIS

In this section, we quantify the effect of clipping in gradient descent and show an example setting where pruning helps reduce this effect.

3.1 Measuring the effect of clipping

One possible way to analyse the change in the gradient step caused due to clipping is to measure the change in direction compared to the true gradient. Intuitively, if the direction doesn't change too much, it can be thought of as taking a smaller step compared to the true gradient in a similar direction. To this end, we observe that the projection of the clipped gradient onto the true gradient can be lower bounded by a quantity which depends on the variance of each dimension over data points and gradient norm. We denote it by R which is defined below.

Definition 3.1. Let $\mathcal{G} = \{\mathbf{g}^{(i)}\}_{i=1}^n$ be per example gradients, with mean $\bar{\mathbf{g}} = \frac{1}{n} \sum \mathbf{g}^{(i)}$. Then define

$$R = \frac{\text{Tr}(\text{Cov}(\mathcal{G}))}{\|\bar{\mathbf{g}}\|^2} = \frac{\frac{1}{n} \sum \|\mathbf{g}^{(i)} - \bar{\mathbf{g}}\|^2}{\|\bar{\mathbf{g}}\|^2} \quad (1)$$

Consider the gradients $\mathbf{g}^{(i)}$ from 3.1. The clipped gradient \mathbf{c} with clipping norm C is the mean of per

example clipped gradients i.e.,

$$\tilde{\mathbf{g}}^{(i)} = \mathbf{g}^{(i)} \cdot \min\left(1, \frac{C}{\|\mathbf{g}^{(i)}\|}\right) \quad (2)$$

$$\mathbf{c} = \frac{1}{n} \sum \tilde{\mathbf{g}}^{(i)} \quad (3)$$

However, to simplify the analysis and based on the empirical observation that most per-example gradients are larger than the clipping norm throughout the training in the standard noise settings of DP-SGD, we make the assumption that $C \leq \|\mathbf{g}^{(i)}\|$ for every i . This simplifies \mathbf{c} to

$$\mathbf{c} = \frac{C}{n} \sum \frac{\mathbf{g}^{(i)}}{\|\mathbf{g}^{(i)}\|} \quad (4)$$

Theorem 3.2. *Assume that $\bar{\mathbf{g}} \neq 0$ and $\mathbf{g}^{(i)} \neq 0$ for all $i = 1, \dots, n$. Let the clipped gradient with clipping norm C be as above and R from 3.1.*

Then

$$\mathbf{c} \cdot \frac{\bar{\mathbf{g}}}{\|\bar{\mathbf{g}}\|} \geq C \left(1 - \frac{R}{2}\right) \quad (5)$$

From 3.2 we can observe that the smaller the ratio R , the more aligned the accumulated clipped gradient is with the actual direction.

3.2 Pruning to improve DPSGD

We construct a theoretical example in which performing pruning clips non-important weights, so that the true target function can still be learned by the pruned model. Later, we confirm empirically that in this scenario pruning reduces R , thereby minimizing the effect of clipping from DP-SGD.

Formally, we consider a binary classification dataset \mathcal{D} , where each example $\mathbf{x}^{(i)}$ is a vector in \mathbb{R}^d , $d = d_s + d_n$, which consists of a signal part and a noise part. The signal part contains a key vector \mathbf{v} which determines the label plus Gaussian noise. The noise part consists of only Gaussian noise. The labels $y^{(i)}$ are drawn from $\{-1, 1\}$.

$$\mathbf{x}^{(i)} = (\mathbf{x}_s^{(i)}, \mathbf{x}_n^{(i)}) \quad (6)$$

$$\mathbf{x}_s^{(i)} \in \mathbb{R}^{d_s}, \mathbf{x}_n^{(i)} \in \mathbb{R}^{d_n} \quad (7)$$

$$\mathbf{x}_s^{(i)} \sim \mathcal{N}(y_i \mathbf{v}, \sigma^2 \mathbf{I}_{d_s}) \quad (8)$$

$$\mathbf{x}_n^{(i)} \sim \mathcal{N}(0, \sigma^2 \mathbf{I}_{d_n}) \quad (9)$$

For simplicity we will consider training on the entire population, but similar results can be obtained for training on a sufficiently large sample using standard concentration inequalities.

Consider training a two layer linear model with hidden layer of size m

$$f(\mathbf{x}) = \mathbf{W}_2 \mathbf{W}_1 \mathbf{x}, \quad (10)$$

$$\mathbf{W}_2 \in \mathbb{R}^{1 \times m}, \mathbf{W}_1 \in \mathbb{R}^{m \times d} \quad (11)$$

to minimize the mean squared error

$$\mathcal{L} = \mathbb{E}_{(\mathbf{x}, y) \sim \mathcal{D}} \left[\frac{1}{2} \|f(\mathbf{x}^{(i)}) - \mathbf{y}^{(i)}\|^2 \right] \quad (12)$$

To aid in our analysis, we decompose

$$\mathbf{W}_1 = (\mathbf{W}_s \quad \mathbf{W}_n) \quad (13)$$

$$\mathbf{W}_s \in \mathbb{R}^{m \times d_s}, \mathbf{W}_n \in \mathbb{R}^{m \times d_n} \quad (14)$$

Intuitively, \mathbf{W}_s consists of connections to the signal part of the input and \mathbf{W}_n consists of connections to the noise part of the input which correspond to non-important weights with regards to pruning.

We will consider clipping the first layer, as clipping the second layer is similar to reducing the dimension of the hidden layer m .

Under this setting, we obtain the following

Theorem 3.3. *Suppose that at initialization the following holds: $\mathbf{W}_2^\top \mathbf{W}_2 = \mathbf{W}_1 \mathbf{W}_1^\top$. Further assume that we train using gradient flow and converge to a global minimum. Then at this point*

$$\mathbf{W}_n = \mathbf{0} \quad (15)$$

The initialization assumption has been used in previous theoretical works ((Arora et al., 2018)). Moreover, the convergence to a global minima is not restrictive as it has been shown that for linear networks all local minima are global minima ((Kawaguchi, 2016)).

In general, this Theorem 3.3 shows that the weights in \mathbf{W}_n are expected to be small, hence will be clipped by magnitude pruning.

4 EXPERIMENTS

In this section we provide empirical evidence for the hypothesized behavior and weaknesses of DP-SGD as discussed above. We also empirically demonstrate the benefits of pruning.

Datasets and Models. All experiments in this section use the publicly available CIFAR10 and CIFAR100 datasets (Krizhevsky et al., 2009) using a Resnet18 model architecture (He et al., 2016). For DP-SGD, the Opacus library (Yousefpour et al., 2021) was used to replace batch normalization layers with group normalization layers, as is required to maintain privacy

guarantees. Experiments were also performed on the LeNet (CNN) (LeCun et al., 1998) architecture to illustrate that behaviors persist across drastically different model sizes (≈ 11 million parameters for Resnet18 vs $\approx 50,000$ for LeNet). Please see the Appendix for further experiments.

Training. Models trained via SGD used batch size 128 and learning rate 0.1 without momentum or data augmentation. Models trained with DP-SGD used batch size 1024 and learning rate 0.5. All models were trained using cross entropy loss on NVIDIA RT2080Ti 11GB GPUs. Reported results are averaged over 3-5 training runs of 30 epochs. All DP-SGD guarantees are for $\delta = 1 \times 10^{-5}$. See the Appendix for detailed descriptions of hyperparameter choices.

Pruning. Magnitude pruning was used to prune each network. Given the initialization point of the model to be pruned, this model was then trained for 20 epochs using the pre-training datasets outlined in Figure 13. For pruning level $p \in [0, 1]$, the smallest $(1-p)$ proportion of weights by magnitude were pruned in each layer. The remaining weights were reset to their initialization values.

4.1 Properties of DP-SGD, SGD and Loss basins in high dimensional spaces

4.1.1 Importance of early Vs late epochs

To test the conjecture in (Ganesh et al., 2023) that the poor performance of DP-SGD arises in the early stages of optimization, we divide the training/optimization process into Phase 1 (k epochs) and Phase 2 ($T - k$ epochs). Two models are trained using SGD and DP-SGD for Phase 1, and then separate copies of each are trained with SGD and DP-SGD for Phase 2.

Figure 2(a) demonstrates the loss results for the CNN model. Clearly, the losses are determined by the mode of operation in Phase 2. The two Phase 2 sequences that use SGD converge rapidly to similar losses, while the SGD-DPSGD sequence has its loss increase to appear at a similar level as the DPSGD-DPSGD sequence. Corresponding test accuracy are shown in Figure 2(b), and results for Resnet18 (Figure 2 c) and d)) show analogous patterns. These results show that contrary to the suggestion in (Ganesh et al., 2023), the early phases are not entirely decisive, and the inability to find a good solution even in a good basin is a major weak point of DP-SGD.

4.1.2 Loss basin dimensions

By carrying out multiple runs of SGD we identify many basin locations with equal levels of loss at the basin floor. Figure 3 shows that the linear mode interpola-

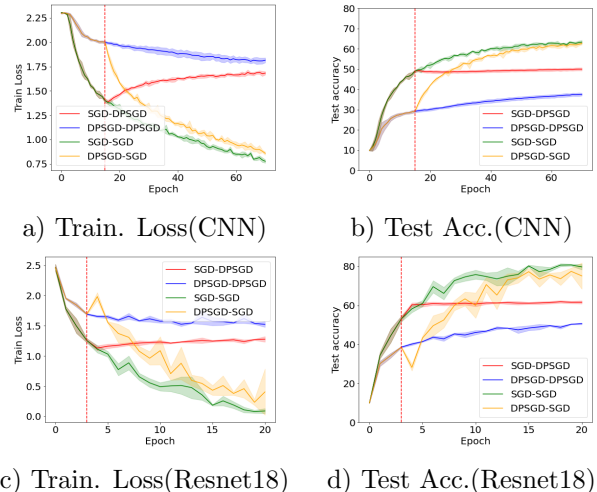


Figure 2: Performance with different Phase 1 and Phase 2 training methods. Later training epochs determine the final performance of both models for CIFAR10. DP-SGD used noise multiplier $\sigma = 0.55$ and maximum gradient norm $C = 1.0$ in each epoch, with $\epsilon \approx 7$ after training. $k = 15$ for CNN and $k = 3$ for Resnet18.

tions between different SGD solutions contain a large barrier in between, suggesting that these are different loss basins, or parts of basins not linearly connected. The basin floors are at equally low loss levels, implying that there are many good solutions and initialization is not decisive.

To further evaluate the shape of the basins, we carried out experiments where two different models (θ_0, θ_1) were trained in Phase 2 starting from the same Phase 1 model with $k = 5$. The linear mode interpolation profile between θ_0 and θ_1 shows an almost flat line, showing that the basin floor is almost flat (Figure 4). On the other hand, the interpolation in a random direction starting from θ_0 shows the loss to rise rapidly. This was observed consistently on 100 random directions, where the maximum cosine similarity between the directions was 0.0012, implying that the directions are mainly orthogonal, as expected when sampling random vectors in high dimensions.

This observation implies that the loss basin floor containing θ_0 and θ_1 is low dimensional compared to the ambient dimension (number of parameters). Any random vector – such as the noise vector generated by DP-SGD – from a model on the basin floor will take the process along a path of steep rise in loss. Note that the dimension of the loss basin itself is not critical to this observation, as long as a number of directions exist where loss increases rapidly.

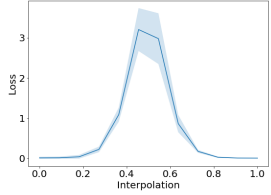


Figure 3: SGD models with different initialization have similar losses (θ_0 at interpolation=0 and θ_1 at interpolation=1) but are not linear mode connected, implying that they are in different basins, or different regions of a non-convex basin.

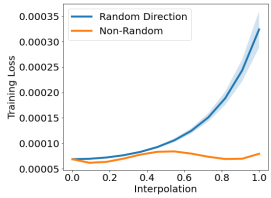


Figure 4: Comparison of the linear mode interpolation profiles of models θ_0, θ_1 in the same linearly connected basin at distance of 15 units, with a model obtained by moving from θ_0 15 units along a random vector in the ambient space. Evaluated with 100 random vectors, with maximum cosine similarity of 0.0012. In random directions, loss increases rapidly.

4.1.3 Comparison of SGD and DP-SGD solutions with linear mode interpolations

The linear interpolation instability for pairs of SGD models trained from the same Phase 1 model (for varying k) is shown in Figure 5(a). Clearly, SGD finds its basin early. However, DP-SGD shows high values of instability, implying that two runs of DP-SGD almost never end in the same linear basin, except perhaps for high values of both k and ϵ . When the two models are trained by SGD and DP-SGD respectively in Phase 2, the differences in loss profile can be seen in Figure 6 – suggesting that the two models do not end in the same basin unless ϵ and k are large. The corresponding results where Phase 1 uses DP-SGD are shown in Figure 7. In this case, since the starting point is at a high loss and far from the basin floor, the Phase 2 DP-SGD always ends in a different basin.

In fact, as shown in Figure 8, If we interpolate the Phase 1 model with Phase 2 model, we see that in all cases, DP-SGD does not stay in the same basin as in Phase 1 ($k = 10$), and always ends at a different basin.

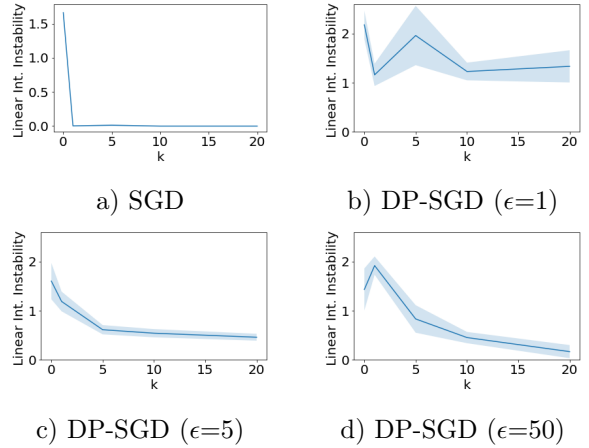


Figure 5: SGD and DP-SGD Instability. Linear interpolation stability is shown using 30 values of α between two models trained with different copies after Phase 1. Higher y-values represent less linear mode stability.

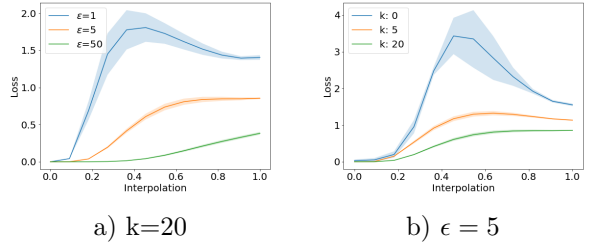


Figure 6: Linear model interpolation between models θ_0 trained for 20 epochs with SGD in Phase 2 and θ_1 trained for 20 epochs with DP-SGD in Phase 2. Phase 1 was trained with SGD.

4.1.4 Comparing Noise and Clipping

We now examine the effects of clipping and noise separately, observing that noise alone does not degrade model performance as larger gradients can be used to recover the unwanted deviations, whereas clipping impacts model performance by slowing progress. The combination of both clipping and noise in DP-SGD is the worst case scenario, where clipping inhibits recovery from the perturbation created by noise.

In Figure 9, we observe the loss and gradient norm for clipped SGD, noisy SGD, DP-SGD and SGD, both at model initialization and later in model training. For a fixed training batch B , we take $t = 5$ steps with clipping set to $C = 1.0$, learning rate 0.1, batch size 128 and a noise scale of 0.4. The mean and average values over batches of size 128 is reported. At initialization in Figure 9 a), SGD achieves the lowest loss. Both clipping and noise reduce loss improvement, but DP-SGD has significantly worse performance than any other method. The gradient norms in Figure 9 b) shed light on this,

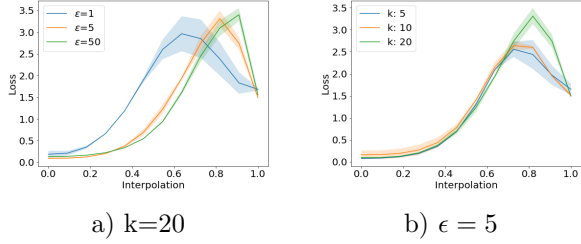


Figure 7: Linear mode interpolation. θ_0 trained for 20 epochs with SGD in Phase 2, and θ_1 trained for 20 epochs with DP-SGD in Phase 2. Phase 1 trained with DP-SGD.

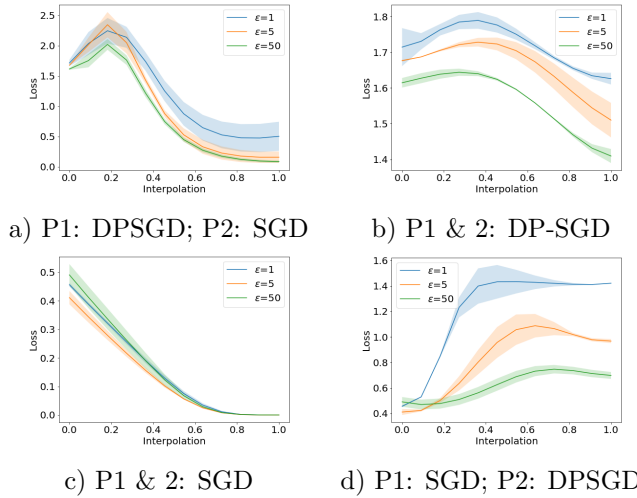


Figure 8: Linear mode interpolation. θ_0 is model at end of Phase 1; θ_1 is model at end of phase 2. SGD Phase 1 followed by also SGD Phase 2 is the only setting where the model clearly stays on the same optimization basin.

with low noisy and DP-SGD gradient norms suggesting that these methods have not located a basin to optimize within quickly.

When we instead begin from a model pre-trained for 10 epochs with SGD, Figure 9 c) shows similar loss trends to an untrained model, but the gradient norm behavior in Figure 9 d) differs. In this case, the gradient norm is largest for DP-SGD and the clipped model, with all variants having a larger gradient norm than SGD. This suggests that clipping as well as noise contributes to gradient norm increases over training, and therefore increased distortion of the true gradient at each step. See the Appendix for a comparison of gradient norms throughout training for DP-SGD vs SGD, the larger gradient norms observed in Figure 9 persist.

Figure 10 shows the accuracy of clipping with maximum gradient norm 1.0 and noise addition with scale 2.4, settings equivalent to those for DP-SGD with $\epsilon = 1$.

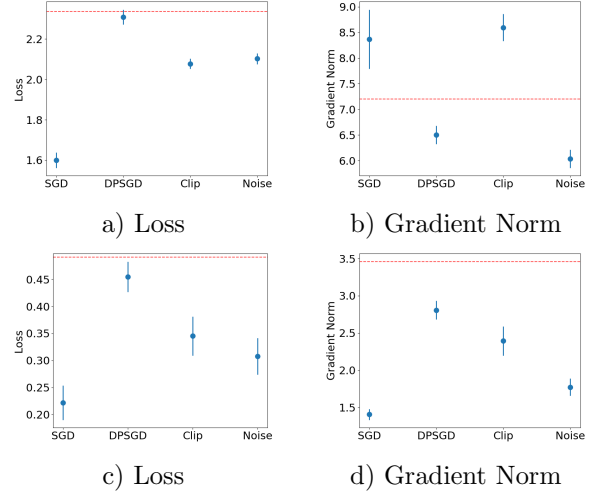


Figure 9: Training loss and gradient norms after 5 training steps with a fixed training batch of size 128. The value before training is shown by the red dashed line. The top row starts training from initialization, the bottom row begins training from a model that has been trained for 10 epochs with SGD.

If we directly compare the effects of noise and clipping for a given learning rate, batch size and number of epochs, then clipping significantly impacts training performance by slowing progress when gradient norms increase after the first few epochs, whereas noisy SGD attains the same final test accuracy as SGD. This further supports the idea that clipping plays a significant role in preventing DP-SGD from recovering from the required noise addition that would otherwise not be detrimental to performance.

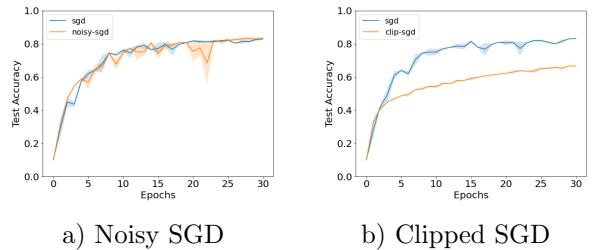


Figure 10: Noisy-SGD Accuracy test accuracy comparison with $\sigma = 2.4$ and Clipped-SGD with maximum gradient norm 1.0 for Resnet18 with Cifar10.

4.2 Pruning

Given the hypothesized benefits of pruning in both reducing the random noise added during DP-SGD training and reducing the impact of clipping, we now test these hypotheses empirically. In Figure 11 we confirm that in the setting described in Section 3.2, pruning re-

duces the ratio R , better aligning the clipped gradient with the original gradient direction.

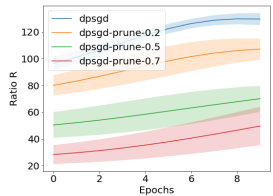


Figure 11: Ratio R reduced by pruning.

This behavior is further evidenced in Figure 12 a) which demonstrates how pruning alleviates the reduction in accuracy caused by clipping SGD for Resnet18, even when there is no noise present. In contrast, Figure 12 b) shows that pruning can help the network to train faster for noisy SGD on Resnet18 but not attain higher test accuracy, note that pruning also helps SGD without noise train more quickly and therefore this behavior is not unique to noisy SGD.

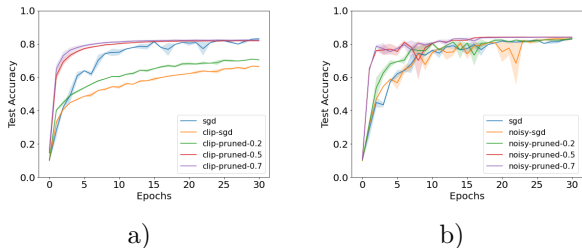


Figure 12: a) Clipped-SGD Test Accuracy comparison with $C = 1.0$ for Resnet18 with Cifar10 pre-training. This clipping scale corresponds to the maximum gradient norm used for $\epsilon = 1$ and $\epsilon = 2$ experiments. b) Noisy-SGD Accuracy comparison with $\sigma = 2.4$. This noise scale corresponds to the noise level for $\epsilon = 1$. Training accuracy plots show the same trends.

Given, these results, the dramatic improvement in test accuracy for DP-SGD with pruning shown Figure 13 is unsurprising, demonstrating that pruning increases DP-SGD accuracy, with the same trend as Figure 11 where 0.7 pruning has the strongest performance. The large improvement of around 23% seen in Figure 13 a) and b) using non-private pruning implies that if pruning can be effectively implemented in a privacy preserving manner the benefits of pruning can be significant. Figure 13 e) and f) shows an example of how to achieve this, by pruning using Cifar100. See (Luo et al., 2021) for further evidence of the potential test accuracy benefits of pruning for DP-SGD test accuracy. Another notable aspect addressed by pruning is that of DP-SGD trained models residing significantly further from the origin than SGD models (e.g. $1.7\times$). In the Appendix we see that pruning reduces this difference, with parameter

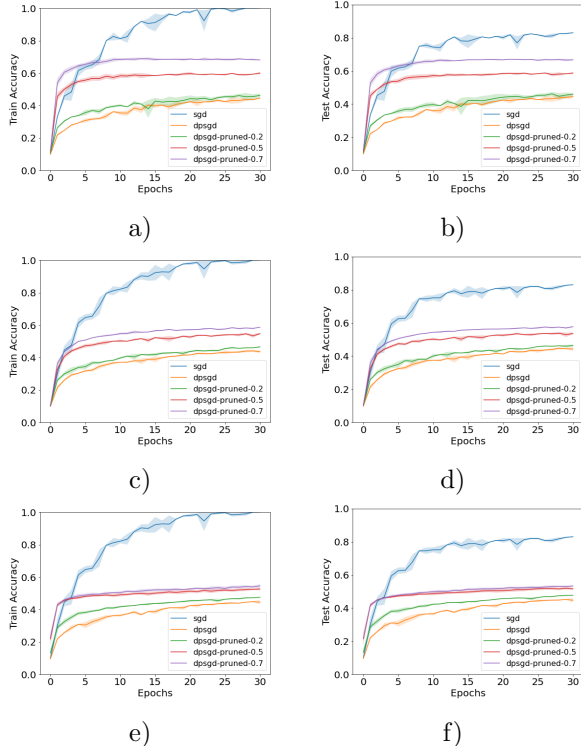


Figure 13: DP-SGD Test Accuracy comparison with $\epsilon = 1$ for Resnet18. Top row: magnitude pruning via non-private Cifar10 Phase 1. Middle row: magnitude pruning via non-private Cifar10 using 5% of Cifar10. Bottom row: magnitude pruning via Cifar100.

distributions for pruned DP-SGD models more closely replicating those of SGD models. See the Appendix for further results, including ablation studies.

5 RELATED WORKS

Since its initial proposal, Differentially Private Stochastic Gradient Descent has been studied for its convergence properties (Abadi et al., 2016; Bassily et al., 2014). More recent theoretical works have studied clipping for its impact on convergence (Xiao et al., 2023; Chen et al., 2020). Theoretical approaches of sparsifying gradients to improve the performance of DP-SGD have been developed, where sparsification is carried out individually for each gradient at runtime (Zhou et al., 2021; Yu et al., 2021). In contrast to gradient sparsification, pruning can be viewed as a one time pre-sparsification of both the network and gradients. Pruning of the normalization layers of Resnet has been found to improve performance of DP-SGD (Luo et al., 2021).

In contrast to these works, we use mechanisms such as Linear mode connectivity (Frankle et al., 2020) to study

the loss basins and make fine grained comparisons of DPSGD models with SGD models. We demonstrate the individual impacts of clipping and noise and the low dimensionality of loss basins, and provide theoretical justifications for pruning.

6 CONCLUSION

This paper has provided several new insights theoretically and experimentally into the operation of DP-SGD. While it does not quite solve the problem of training private models that are almost as good as non-private ones, the insights from this research should help us to develop better private training algorithms in future.

References

- Abadi, M., Chu, A., Goodfellow, I., McMahan, H. B., Mironov, I., Talwar, K., and Zhang, L. (2016). Deep learning with differential privacy. In *Proceedings of the 2016 ACM SIGSAC conference on computer and communications security*, pages 308–318.
- Arora, S., Cohen, N., and Hazan, E. (2018). On the optimization of deep networks: Implicit acceleration by overparameterization. In *International Conference on Machine Learning*, pages 244–253. PMLR.
- Bassily, R., Smith, A., and Thakurta, A. (2014). Private empirical risk minimization: Efficient algorithms and tight error bounds. In *2014 IEEE 55th annual symposium on foundations of computer science*, pages 464–473. IEEE.
- Carlini, N., Liu, C., Erlingsson, Ú., Kos, J., and Song, D. (2019). The secret sharer: Evaluating and testing unintended memorization in neural networks. In *28th USENIX Security Symposium (USENIX Security 19)*, pages 267–284.
- Chen, X., Wu, S. Z., and Hong, M. (2020). Understanding gradient clipping in private sgd: A geometric perspective. *Advances in Neural Information Processing Systems*, 33:13773–13782.
- Dwork, C. (2006). Differential privacy. In *Automata, Languages and Programming*, pages 1–12. ICALP.
- Dwork, C., McSherry, F., Nissim, K., and Smith, A. (2006). Calibrating noise to sensitivity in private data analysis. In *Theory of Cryptography: Third Theory of Cryptography Conference, TCC 2006, New York, NY, USA, March 4-7, 2006. Proceedings 3*, pages 265–284. Springer.
- Frankle, J., Dziugaite, G. K., Roy, D., and Carbin, M. (2020). Linear mode connectivity and the lottery ticket hypothesis. In *International Conference on Machine Learning*, pages 3259–3269. PMLR.
- Fredrikson, M., Jha, S., and Ristenpart, T. (2015). Model inversion attacks that exploit confidence information and basic countermeasures. In *Proceedings of the 22nd ACM SIGSAC conference on computer and communications security*, pages 1322–1333.
- Ganesh, A., Haghifam, M., Nasr, M., Oh, S., Steinke, T., Thakkar, O., Thakurta, A. G., and Wang, L. (2023). Why is public pretraining necessary for private model training? In *International Conference on Machine Learning*, pages 10611–10627. PMLR.
- Garipov, T., Izmailov, P., Podoprikin, D., Vetrov, D. P., and Wilson, A. G. (2018). Loss surfaces, mode connectivity, and fast ensembling of dnns. *Advances in neural information processing systems*, 31.
- He, K., Zhang, X., Ren, S., and Sun, J. (2016). Deep residual learning for image recognition. In *Proceedings of the IEEE conference on computer vision and pattern recognition*, pages 770–778.
- Kawaguchi, K. (2016). Deep learning without poor local minima.
- Krizhevsky, A., Hinton, G., et al. (2009). Learning multiple layers of features from tiny images.
- LeCun, Y., Bottou, L., Bengio, Y., and Haffner, P. (1998). Gradient-based learning applied to document recognition. *Proceedings of the IEEE*, 86(11):2278–2324.
- Li, X., Liu, D., Hashimoto, T. B., Inan, H. A., Kulkarri, J., Lee, Y.-T., and Guha Thakurta, A. (2022). When does differentially private learning not suffer in high dimensions? *Advances in Neural Information Processing Systems*, 35:28616–28630.
- Luo, Z., Wu, D. J., Adeli, E., and Fei-Fei, L. (2021). Scalable differential privacy with sparse network fine-tuning. In *Proceedings of the IEEE/CVF Conference on Computer Vision and Pattern Recognition*, pages 5059–5068.
- Nasr, M., Shokri, R., and Houmansadr, A. (2019). Comprehensive privacy analysis of deep learning: Passive and active white-box inference attacks against centralized and federated learning. In *2019 IEEE symposium on security and privacy (SP)*, pages 739–753. IEEE.
- Papernot, N., Thakurta, A., Song, S., Chien, S., and Erlingsson, Ú. (2021). Tempered sigmoid activations for deep learning with differential privacy. In *Proceedings of the AAAI Conference on Artificial Intelligence*, volume 35, pages 9312–9321.
- Shokri, R., Stronati, M., Song, C., and Shmatikov, V. (2017). Membership inference attacks against machine learning models. In *2017 IEEE symposium on security and privacy (SP)*, pages 3–18. IEEE.

-
- Xiao, H., Rasul, K., and Vollgraf, R. (2017). Fashion-mnist: a novel image dataset for benchmarking machine learning algorithms. *CoRR*, abs/1708.07747.
- Xiao, H., Xiang, Z., Wang, D., and Devadas, S. (2023). A theory to instruct differentially-private learning via clipping bias reduction. In *2023 IEEE Symposium on Security and Privacy (SP)*, pages 2170–2189. IEEE Computer Society.
- Yousefpour, A., Shilov, I., Sablayrolles, A., Testuggine, D., Prasad, K., Malek, M., Nguyen, J., Ghosh, S., Bharadwaj, A., Zhao, J., et al. (2021). Opacus: User-friendly differential privacy library in pytorch. *arXiv preprint arXiv:2109.12298*.
- Yu, D., Zhang, H., Chen, W., and Liu, T.-Y. (2021). Do not let privacy overbill utility: Gradient embedding perturbation for private learning. In *International Conference on Learning Representations*.
- Zhou, Y., Wu, S., and Banerjee, A. (2021). Bypassing the ambient dimension: Private {sgd} with gradient subspace identification. In *International Conference on Learning Representations*.

7 Appendix

Proof of Theorem 3.2. Decompose $\mathbf{g}_i = a_i \frac{\bar{\mathbf{g}}}{\|\bar{\mathbf{g}}\|} + b_i \mathbf{u}_i$, where \mathbf{u}_i is a unit vector orthogonal to $\bar{\mathbf{g}}$. Then the desired inequality becomes

$$\frac{1}{n} \sum_{i=1}^n \frac{a_i}{\sqrt{a_i^2 + b_i^2}} \geq 1 - \frac{\frac{1}{n} \sum_{i=1}^n a_i^2 + b_i^2 - \bar{a}^2}{2\bar{a}^2} \quad (16)$$

where \bar{a} is shorthand for $\frac{1}{n} \sum_{i=1}^n a_i$, and we know $\bar{a} > 0$.

Define the function f by

$$f(a_1, \dots, a_n, b_1, \dots, b_n) = \frac{2}{n} \sum_{i=1}^n \frac{a_i}{\sqrt{a_i^2 + b_i^2}} + \frac{1}{n\bar{a}^2} \left(\sum_{i=1}^n a_i^2 + b_i^2 \right) \quad (17)$$

For any $0 < \alpha < 3\alpha < \beta, 0 < \gamma$, let $J_\alpha = \{(a_1, \dots, a_n, b_1, \dots, b_n) \in \mathbb{R}^{2n} : \bar{a} \geq \alpha\}$ and let $I_{\alpha, \beta, \gamma} = J_\alpha \cap (([-\beta, -\alpha] \cup [\alpha, \beta])^n \times [-\gamma, \gamma]^n)$. We claim that $f \geq 3$ on $I_{\alpha, \beta, \gamma}$. Since $I_{\alpha, \beta, \gamma}$ is compact, f has a minimum on $I_{\alpha, \beta, \gamma}$. It suffices to consider the critical points f and the boundary of $I_{\alpha, \beta, \gamma}$.

We first find the critical points of f . For such critical points, calculate that

$$\frac{\partial f}{\partial a_j} = \frac{2}{n} \frac{b_j^2}{(a_j^2 + b_j^2)^{\frac{3}{2}}} + \frac{2a_j}{n\bar{a}^2} - \frac{2}{n^2\bar{a}^3} \left(\sum_{i=1}^n a_i^2 + b_i^2 \right) = 0 \quad (18)$$

$$\frac{\partial f}{\partial b_j} = -\frac{2}{n} \frac{a_j b_j}{(a_j^2 + b_j^2)^{\frac{3}{2}}} + \frac{2b_j}{n\bar{a}^2} = 0 \quad (19)$$

Suppose that $b_{k_1} = b_{k_2} = 0$ for some k_1, k_2 . Then we must have

$$\frac{2a_{k_1}}{n\bar{a}^2} - \frac{2}{n^2\bar{a}^3} \left(\sum_{i=1}^n a_i^2 + b_i^2 \right) = \frac{2a_{k_2}}{n\bar{a}^2} - \frac{2}{n^2\bar{a}^3} \left(\sum_{i=1}^n a_i^2 + b_i^2 \right) \quad (20)$$

which implies that $a_{k_1} = a_{k_2} = A_1$ for some constant A_1 .

Suppose that for some $k, b_k \neq 0$. Then equation 19 implies that

$$\bar{a}^2 a_k = (a_k^2 + b_k^2)^{\frac{3}{2}} \quad (21)$$

which also implies

$$b_k^2 = \bar{a}^{\frac{4}{3}} a_k^{\frac{2}{3}} - a_k^2 \quad (22)$$

Substituting into Equation 18,

$$0 = \frac{2}{n} \cdot \frac{\bar{a}^{\frac{4}{3}} a_k^{\frac{2}{3}} - a_k^2}{\bar{a}^2 a_k} + \frac{2a_k}{n\bar{a}^2} - \frac{2}{n^2\bar{a}^3} \left(\sum_{i=1}^n a_i^2 + b_i^2 \right) \quad (23)$$

$$= \frac{2}{n\bar{a}^2} \left(\frac{\bar{a}^{\frac{4}{3}} a_k^{\frac{2}{3}}}{a_k} \right) - \frac{2}{n^2\bar{a}^3} \left(\sum_{i=1}^n a_i^2 + b_i^2 \right) \quad (24)$$

$$= \frac{2}{n\bar{a}^{\frac{2}{3}} a_k^{\frac{1}{3}}} - \frac{2}{n^2\bar{a}^3} \left(\sum_{i=1}^n a_i^2 + b_i^2 \right) \quad (25)$$

It follows that for any k_1, k_2 with $b_{k_1}, b_{k_2} \neq 0$, we must have $a_{k_1} = a_{k_2} = A_2$ for some constant A_2 . Moreover, we must have $\frac{2}{n\bar{a}^{\frac{2}{3}} A_2^{\frac{1}{3}}} = \frac{2A_1}{n\bar{a}^2}$ which gives

$$A_1^3 A_2 = \bar{a}^4 \quad (26)$$

Consider two cases. If all the a_i are equal, then $a_i = A_1 = A_2 = \bar{a} > 0$, and also

$$b_i^2 = \bar{a}^{\frac{4}{3}} a_i^{\frac{2}{3}} - a_i^2 = 0, \quad (27)$$

so $b_i = 0$ for all i . One can check that f at such a point is equal to 3.

Now suppose for the sake of contradiction not all the a_i are equal. The one of them, WLOG let it be a_1 , satisfies $a_1 > \bar{a}$. Then $a_1 \bar{a}^2 < (a_1^2 + b_1^2)^{\frac{3}{2}}$, so the only way Equation 19 is satisfied is if $b_1 = 0$. But then $a_1 = A_1$. It follows from Equation 26 $0 < A_2 < \bar{a} < A_1$.

Now let n_1 be the number of a_i equal to A_1 and A_2 . We must have

$$\bar{a} = \frac{n_1}{n} A_1 + \left(1 - \frac{n_1}{n}\right) A_2 \quad (28)$$

$$= \frac{n_1}{n} A_1 + \left(1 - \frac{n_1}{n}\right) \frac{\bar{a}^4}{A_1^3} \quad (29)$$

Set $\lambda = \frac{A_1}{\bar{a}} > 1$. Then

$$1 = \frac{n_1}{n} \lambda + \left(1 - \frac{n_1}{n}\right) \frac{1}{\lambda^3} \quad (30)$$

$$(\lambda^3 - 1) = (\lambda^4 - 1) \frac{n_1}{n} \quad (31)$$

$$\frac{n_1}{n} = \frac{\lambda^3 - 1}{\lambda^4 - 1} \quad (32)$$

Now evaluating f ,

$$f(a_1, \dots, a_n, b_1, \dots, b_n) = \frac{2}{n} \left(n_1 + n_2 \frac{A_2}{A_2^{\frac{1}{3}} \bar{a}^{\frac{2}{3}}} \right) + \frac{1}{n \bar{a}^2} \left(n_1 A_1^2 + A_2^{\frac{2}{3}} \bar{a}^{\frac{4}{3}} \right) \quad (33)$$

$$= 2 \left(\frac{\lambda^3 - 1}{\lambda^4 - 1} + \left(1 - \frac{\lambda^3 - 1}{\lambda^4 - 1}\right) \frac{1}{\lambda^2} \right) + \left(\frac{\lambda^3 - 1}{\lambda^4 - 1} \lambda^2 + \left(1 - \frac{\lambda^3 - 1}{\lambda^4 - 1}\right) \frac{1}{\lambda^2} \right) \quad (34)$$

It is not hard to show that the RHS is greater than 3 for $\lambda > 1$. Thus we have shown that $f \geq 3$ at all critical points.

It remains to check the boundary points. Notice that the dominant term in f as $|b_i| \rightarrow \infty$ is b_i^2 . Hence using sufficiently large γ guarantees that no point with $b_i = \gamma$ for some i can be a minimum. On the other hand, suppose of the a_i take a boundary value. We consider a few cases:

Case 1: $a_i = -\beta$. If $b_i \neq 0$, then $\frac{\partial f}{\partial b_i} \neq 0$, so we can adjust b_i to decrease f . If $b_i = 0$, then 18 shows that increasing a_i will decrease the value of f .

Case 2: If the only boundary values are of the form $a_i = \pm\alpha$ observe that f is scale-invariant, so scaling all inputs by $1 + \delta$ shows that f has the same value at some interior point of $I_{\alpha, \beta, \gamma}$, which we already know is not a minimum or greater than 3.

Case 3: a_i on the boundary are only of the form $a_i = \beta$. A similar argument as the previous case but scaling down works.

Case 4: Some $a_i = \alpha$ and some $a_j = \beta$. But then from Equation 18 we see that $\frac{\partial f}{\partial a_i} < \frac{\partial f}{\partial a_j}$, so either $\frac{\partial f}{\partial a_i} < 0$ or $\frac{\partial f}{\partial a_j} > 0$. This means that either increasing a_i or decreasing a_j decreases the value of f , so this cannot be a minimum.

Case 5: Some $a_i = -\alpha$ and some $a_j = \beta$. If $b_i \neq 0$ then $\frac{\partial f}{\partial b_i} \neq 0$ by 19 and we can adjust b_i appropriately to decrease f . A similar argument handles the case that $b_j \neq 0$.

Suppose $b_i = b_j = 0$. Set $a'_i = \alpha, a'_j = \beta - 2\alpha$. Then

$$f(a_1, \dots, a'_i, \dots, a'_j, \dots, a_n, b_1, \dots, b_n) - f(a_1, \dots, a_n, b_1, \dots, b_n) = \frac{2}{n} (1 - (-1)) + \frac{1}{n \bar{a}^2} ((\beta - 2\alpha)^2 - \beta^2) \quad (35)$$

$$= \frac{4}{n} \left(1 - \frac{\beta(\beta - \alpha)}{\bar{a}^2} \right) \quad (36)$$

Taking $\beta > n\alpha$ guarantees that $\beta > \beta - \alpha > \bar{a}$, so for β sufficiently large the RHS is less than 0, showing that the original point is not a minimum.

The final boundary condition is if $\bar{a} = \alpha$. We have already considered the condition where any of the a_i are equal to $\pm\alpha$, so the only way this is possible if there exists some i s.t. $a_i < -\alpha$. If $b_i \neq 0$, we can decrease $|b_i|$ to decrease f by 19. If $b_i = 0$, then 18 shows that increasing α_i will decrease the value of f . Thus such a point cannot be a minimum. This proves that $f \geq 3$ on $I_{\alpha,\beta,\gamma}$.

Now since α, β, γ work for any β, γ sufficiently large, we conclude that $f \geq 3$ on $\{(a_1, \dots, a_n, b_1, \dots, b_n) \in \mathbb{R}^{2n} : \bar{a} > 0\} \cap ((\mathbb{R} \setminus \{0\})^n \times \mathbb{R}^n)$. We can extend to the possibility that some of the a_i are zero by continuity. This completes the proof. \square

Proof of 3.3. Collect the input examples into a matrix $\mathbf{X} = [x^{(1)}, \dots, x^{(n)}]$ and let $\mathbf{Z} = f(\mathbf{X}) \in \mathbb{R}^{1 \times n}$ be the matrix of model outputs on the dataset. Then the gradients are

$$\begin{aligned}\frac{\partial \mathcal{L}}{\partial \mathbf{W}_1} &= \mathbf{W}_2^\top \frac{\partial \mathcal{L}}{\partial \mathbf{Z}} \mathbf{X}^\top \\ \frac{\partial \mathcal{L}}{\partial \mathbf{W}_2} &= \frac{\partial \mathcal{L}}{\partial \mathbf{Z}} \mathbf{X}^\top \mathbf{W}_1^\top\end{aligned}$$

In addition, observe that using the rule of gradient flow,

$$\begin{aligned}\frac{d}{dt}(\mathbf{W}_1 \mathbf{W}_1^\top) &= \mathbf{W}_1 \left(\frac{d\mathbf{W}_1}{dt} \right)^\top + \frac{d\mathbf{W}_1}{dt} \mathbf{W}_1^\top \\ &= -\mathbf{W}_1 \left(\frac{\partial \mathcal{L}}{\partial \mathbf{W}_1} \right)^\top - \frac{\partial \mathcal{L}}{\partial \mathbf{W}_1} \mathbf{W}_1^\top \\ \frac{d}{dt}(\mathbf{W}_2^\top \mathbf{W}_2) &= \mathbf{W}_2 \left(\frac{d\mathbf{W}_2}{dt} \right)^\top + \frac{d\mathbf{W}_2}{dt} \mathbf{W}_2^\top \\ &= -\left(\frac{\partial \mathcal{L}}{\partial \mathbf{W}_2} \right)^\top \mathbf{W}_2 - \mathbf{W}_2^\top \frac{\partial \mathcal{L}}{\partial \mathbf{W}_2}.\end{aligned}$$

Substituting, we see that $\frac{d}{dt}(\mathbf{W}_1 \mathbf{W}_1^\top) = \frac{d}{dt}(\mathbf{W}_2^\top \mathbf{W}_2)$. Since we assumed that $\mathbf{W}_1 \mathbf{W}_1^\top = \mathbf{W}_2^\top \mathbf{W}_2$, it follows that equality holds throughout training.

Now the model is linear in $\mathbf{W} = \mathbf{W}_2 \mathbf{W}_1$, so by well known results on linear regression, the optimal model $\mathbf{W}_2^* \mathbf{W}_1^*$ on the entire dataset satisfies

$$\begin{aligned}\mathbf{W}_2^* \mathbf{W}_1^* &= \mathbb{E}_{\mathbf{x} \sim \mathcal{D}}[y \mathbf{x}^\top] (\mathbb{E}_{\mathbf{x} \sim \mathcal{D}}[\mathbf{x} \mathbf{x}^\top])^\dagger \\ &= \mathbf{v}^\top (\mathbf{v} \mathbf{v}^\top + \sigma^2 \mathbf{I})^\dagger \\ &= \frac{\|\mathbf{v}\|}{\|\mathbf{v}\|^2 + \sigma^2} \mathbf{v}^\top\end{aligned}$$

Combined with the fact that $\mathbf{W}_1^* (\mathbf{W}_1^*)^\top = (\mathbf{W}_2^*)^\top \mathbf{W}_2^*$, it follows that $\mathbf{W}_1^*, \mathbf{W}_2^*$ are both rank 1 matrices with singular value $\sqrt{\frac{\|\mathbf{v}\|}{\|\mathbf{v}\|^2 + \sigma^2}}$, and the left singular vector of \mathbf{W}_1^* corresponds to the right singular vector of \mathbf{W}_2^* . In particular,

$$\mathbf{W}_1^* = \sqrt{\frac{1}{\|\mathbf{v}\|(\|\mathbf{v}\|^2 + \sigma^2)}} \boldsymbol{\alpha} \mathbf{v}^\top \tag{37}$$

$$\mathbf{W}_2^* = \sqrt{\frac{\|\mathbf{v}\|}{\|\mathbf{v}\|^2 + \sigma^2}} \boldsymbol{\alpha}^\top \tag{38}$$

for some unit vector $\boldsymbol{\alpha} \in \mathbb{R}^m$. From this expression it is easy to see that $\mathbf{W}_n^* = \mathbf{0}$. \square

8 Experimental Details

We now outline further experimental results and provide further details about experiments included in the main body of text.

Previous Experiment Details: In Figure 13 c), the Cifar100 Resnet18 model used to prune the model was trained using SGD with data augmentation (horizontal flipping and random cropping), momentum=0.9, learning rate 0.02 and batch size 512 for 100 epochs. For DP-SGD, unless σ is explicitly stated, then σ has been calculated automatically by the Opacus package for the fixed ϵ and δ values reported using the `make_private_with_epsilon` function.

Additional Models and Datasets: In this section, in addition to Cifar10 and Cifar100 as used previously, we also provide results using the MNIST (LeCun et al., 1998) and FashionMNIST (Xiao et al., 2017) datasets. Table 1 shows hyperparameters for SGD and DP-SGD variants of the model and dataset combinations included in this Appendix. Hyperparameters described in Table 1 were selected via hyperparameter sweeps for DP-SGD and SGD with learning rates $\{0.01, 0.05, 0.1, 0.5, 1.0\}$ and batch sizes $\{32, 64, 128, 512, 1024\}$. Pruned variants were then trained using the same fixed hyperparameters.

Model	Dataset	SGD		DP-SGD	
		η	Batch Size	η	Batch Size
CNN (LeNet)	MNIST	0.1	128	1.0	512
	FashionMNIST	0.1	64	0.5	512

Table 1: Hyperparameter choices for experiments included in this section

9 Further Experiments

Further results for Resnet18: Figures 14 demonstrates the performance of pruning for Cifar10 and Resnet18 with $\epsilon = 2$. As with $\epsilon = 1$, pruning using non-private pre-training on Cifar10 results in the highest final test accuracy for DP-SGD with a pruning proportion of 0.7. As before, pruning using Cifar100 or 5% of Cifar10 also improves the test accuracy of the model.

Pruning percentages: Figure 15 shows that for Cifar10 and Resnet18, increasing the pruning proportion past 0.7 does not further improve performance.

Parameter and Gradient Norm Distributions: Gradient norms are larger during training for DP-SGD in comparison to SGD, as seen in Figure 16. This will result in more severe clipping of the gradient than would otherwise have been necessary. Figure 17 shows that pruned DP-SGD models better replicate the parameter distribution of SGD models. DP-SGD models have significantly fewer parameters close to 0 than SGD models, their L2 distance from the origin is correspondingly around $1.7\times$ larger. Pruning reduces this to $1.2\times$ larger.

Other Models and Datasets: In Figures 18 and 19 we demonstrate that magnitude pruning increases the test accuracy of DP-SGD for a significantly smaller model (LeNet) using both the MNIST and FashionMNIST tasks.

Varying the Phase 1 Training Duration: In Figure 20, we provide examples of different lengths of Phase 1 training (k) from Figure 2. In all cases we see similar trends, with the DP-SGD model under-performing in comparison to SGD during the first few epochs, but also negatively impacting model performance later in training (Phase 2) when the model is initially trained with SGD.

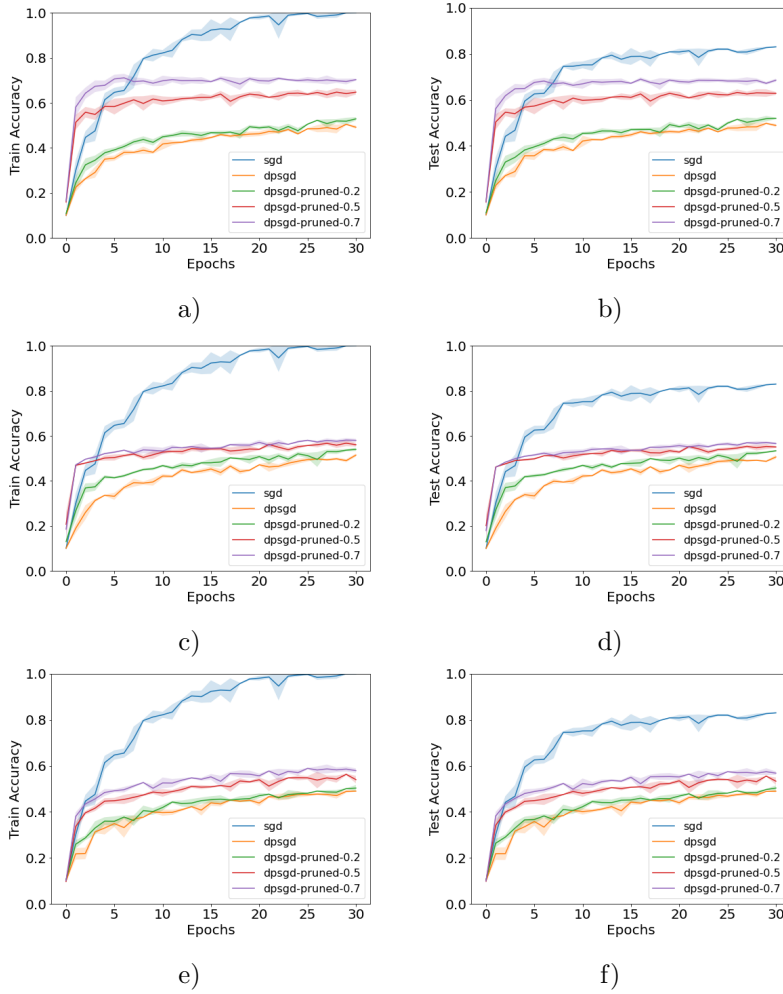


Figure 14: DPSGD Test Accuracy comparison with $\epsilon = 2$ for Resnet18 with Cifar10. a) and b) show pruning via non-private training with Cifar10 c) and d) show pruning via non-private training with 5% of Cifar10. e) and f) show pruning via training with Cifar100.

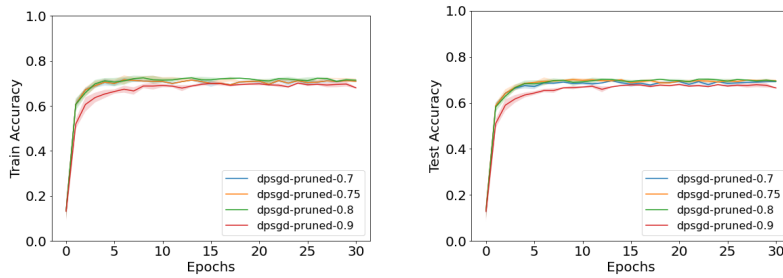
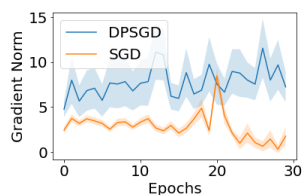
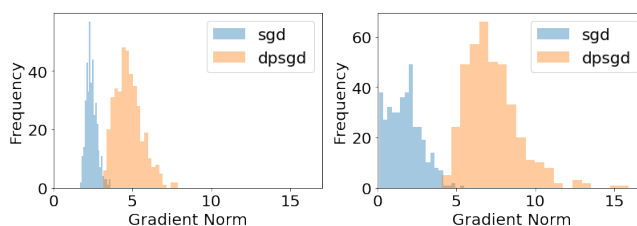


Figure 15: Sweep over higher pruning percentages for Cifar10 and Resnet18.



(a)



(b)

(c)

Figure 16: Top row: Average gradient norm over training data batches of size 128 for SGD vs DP-SGD with Resnet18 and Cifar10. Bottom row: histogram comparisons of the gradient norms after 1 epoch of training (b) and 30 epochs of training (c).

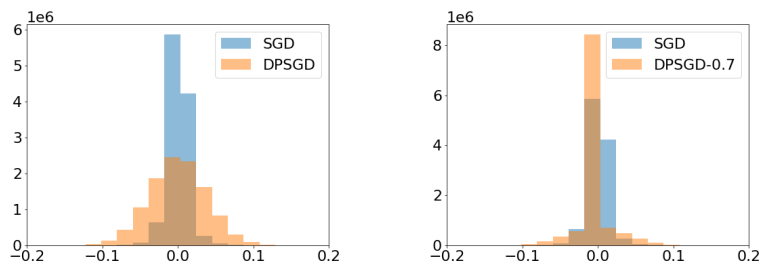


Figure 17: DP-SGD models for $\epsilon = 1$ have fewer parameters closer to 0 than SGD models, implying again that they occupy different regions of the parameter space. We find that SGD models have an L2 distance from the origin of 86 ± 0.5 in comparison to 142 ± 0.01 for DP-SGD models. With pruning the DP-SGD distance reduces to 100 ± 0.02 .

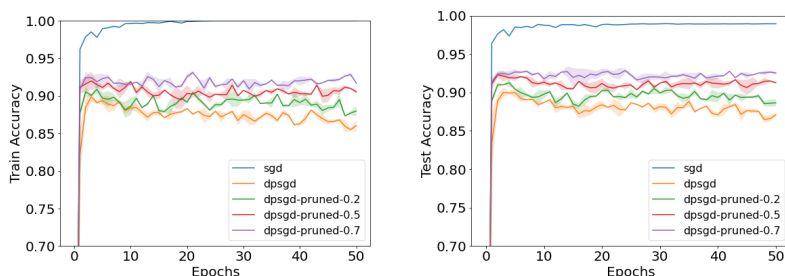


Figure 18: Training and test accuracies for a CNN (LeNet) model with MNIST for $\epsilon = 1$. Magnitude pruning performed via pre-training with MNIST.

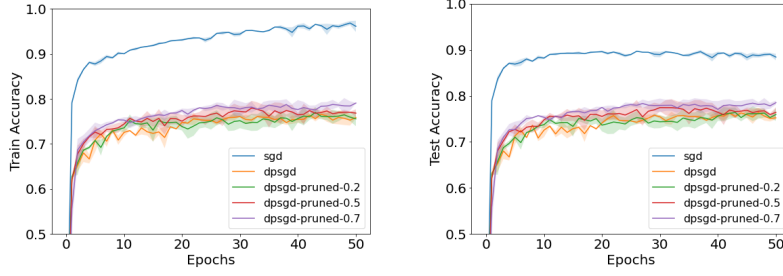


Figure 19: Training and test accuracies for a CNN (LeNet) model with FashionMNIST for $\epsilon = 1$. Magnitude pruning performed via pre-training with FashionMNIST.

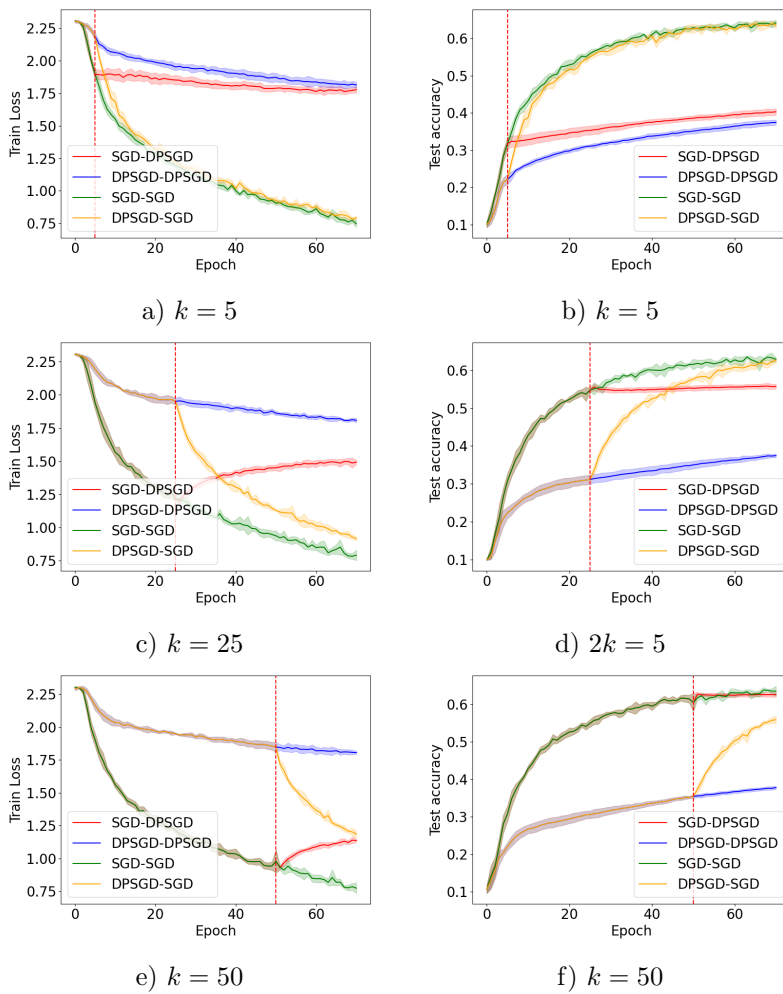


Figure 20: Performance with different Phase 1 and Phase 2 training methods. Later training epochs determine the final performance of both models for CIFAR10. DP-SGD used noise multiplier $\sigma = 0.55$ and maximum gradient norm $C = 1.0$ in each epoch, with $\epsilon \approx 7$ after training.